Remote defect detection of FRP-bonded concrete system using acoustic-laser and imaging radar techniques

Tzuyang Yu [a], Tin Kei Cheng [b], Ao Zhou [b], Denvid Lau [b],*

[a] Department of Civil and Environmental Engineering, The University of Massachusetts Lowell, Lowell, MA 01854, USA
[b] Department of Architecture and Civil Engineering, City University of Hong Kong, Hong Kong, China

HIGHLIGHTS

- A nondestructive testing scheme combining acoustic-laser and imaging radar techniques is proposed.
- The defect characterization of FRP-bonded concrete structure is conducted.
- Both global and local response of FRP-bonded concrete structure are evaluated.
- The structural health can be monitored effectively by the proposed detection scheme.

GRAPHICAL ABSTRACT
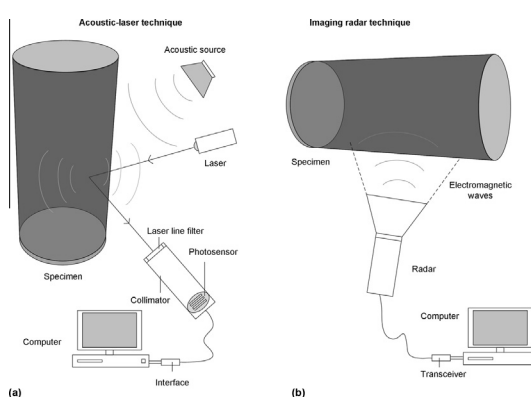
ARTICLE INFO

ABSTRACT

Two different remote nondestructive testing (NDT) techniques, the acoustic-laser and imaging radar techniques, are studied for near-surface defect detection in fiber-reinforced polymer (FRP) retrofitted systems. In the acoustic-laser technique, the targeted structure is excited by acoustic waves, while vibration data on a measurement point is remotely collected. In the imaging radar technique, radar signals (electromagnetic waves) are remotely emitted toward the target structure and measured when they are reflected from the structure. Three FRP-bonded concrete cylinders with various defect sizes were fabricated for laser and radar measurements. The pros and cons of these two techniques are described with the support of experimental result.

1. Introduction

Maintenance of aging concrete structures (reinforced and prestressed) is one of the greatest challenges faced by the civil engineering profession, as well as many nations worldwide. Strengthening and repair of these deteriorated structures has become an economic approach over reconstruction, especially for short-term, immediate response to the aging infrastructure problem. A number of strengthening and repair technologies have been developed and applied for extending the service life of concrete structures by means of restoring their design capacity and preserving their structural redundancy. The use of fiber-reinforced polymer (FRP) composites as an externally bonded element to confine the concrete in order to secure the integrity of concrete structures has been proven, both theoretically and practically, to be an

* Corresponding author.
  E-mail address: denvid@mit.edu (D. Lau).

effective and efficient strengthening/repair approach. FRP strengthening system should be designed such that a brittle failure due to the FRP rupture can be avoided. Both the Canadian and American design codes are based on the principle of limit state design. This method can provide an acceptable safety margin for both the serviceability limit state (excess results in excessive deflections and cracking) and the ultimate limit state (excess results in failure, stress rupture, and fatigue) [1,2]. FRP strengthening should be designed according to strength and serviceability requirements as stated in the ACI (American Concrete Institute) 318 Building Code Requirement for Structural Concrete [3]. The structures should be carefully monitored and evaluated to ensure that a considerable improvement of load bearing capacity is obtained after FRP strengthening. The service conditions of FRP systems including loading conditions and environmental considerations play an important role in the long-term performance of FRP systems. Certain loading types, such as impact loading, sustained loading and cyclic loading, should be carefully considered. It is noted that the mechanical properties of FRP degrade under various environmental effects, such as alkalinity/acidity, ultraviolet light, high temperature and high humidity. Hence both the design ultimate tensile strength and design rupture strain should be evaluated with the consideration of the long-term loading and environmental factors.

Integrating a new FRP composite with the concrete substrate results in a multi-layer structural system whose damage mechanism is different from conventional concrete structures. Various approaches on the modeling of debonding have been proposed using both strength and fracture approaches [4–6]. Focusing on the strength-based approach, a new theoretical model has been proposed based on the numerical integration method to evaluate the stress–strain curve of an FRP-wrapped concrete column [7]. In design-oriented models, the stress–strain relationship of FRP-wrapped concrete is predicted by closed-form equations on the basis of experimental interpretation. In analysis-oriented models, the stress–strain curve of FRP-confined concrete is obtained through an incremental numerical procedure [8,9]. However, in all the above-mentioned models, there is a lack of understanding on the effect of defect towards the global structural behavior of an FRP-wrapped concrete column, in which such scenario always happens in reality. In the behavior of FRP-bonded concrete systems, construction defects and structural/environmental damages may occur within the FRP-bonded concrete structures, especially in the vicinity of FRP-concrete interface. Construction defects such as trapped air voids or pockets can occur between FRP sheets/-plates and the concrete substrate during construction. These air voids serve as a region with shear stress discontinuities, as well as the location of stress concentration, leading to further development of delamination in the interface region and debonding of FRP from the concrete substrate. Structural damages such as concrete cracking or crumbling inside the FRP wrapping, and/or debonding of the FRP sheet from concrete could also occur under various levels of confinement pressure provided by the FRP wrap. These types of failure have been observed in FRP-wrapped concrete specimens [10], and also in FRP-wrapped large scale reinforced concrete structures [11,12]. Furthermore, multiple failure modes, e.g. rupture of FRP composites and shear failure, have been found in FRP-wrapped concrete columns. Therefore, detecting the presence of delamination and debonding in the interface between FRP and concrete in order to avoid brittle failures of the multilayer system is important for the safety and durability of FRP-concrete structures.

Although visual inspection of FRP-concrete structures may be sufficient in some scenarios, remote nondestructive testing (NDT) becomes an attractive approach when (i) automation is desired, (ii) quantifiable measurement is required, (iii) access to the structure is difficult, (iv) the FRP surface is concealed by paint, or (v) labor cost for manual inspection is high. In this paper, a combination of acoustic-laser and imaging radar NDT techniques is applied for near-surface inspections of the artificially damaged FRP-bonded concrete system. FRP debonding is modeled by the insertion of an artificial air gap at the FRP-concrete interface. Measurements are first conducted independently using each technique on the same set of specimens. The results are then compared so as to devise possible methods how the two techniques can work together, and to explore potential benefits the combined measurement will provide over using each technique alone. The efficacies of these two techniques, both individually and combined, are investigated in the context of debonding detection and characterization. The synergy of these two techniques can cover a wide range of debonding scenarios. It is envisioned that this synergy can inspire future research to develop combined NDT techniques, which can maintain the strength of each technique and minimize the weaknesses through a combined hybrid approach.

2. Review of existing techniques for remote debonding detection

Knowing that FRP is a critical load-bearing component in retrofitted concrete structures, various NDT approaches are being developed to assess its well-being by detecting debonding and delamination in FRP-concrete structures. Current NDT techniques developed for civil engineering applications include the use of pressure wave, infrared thermography (IRT), radar, and X-ray radiography [13–18]. However, these techniques are not specifically designed for the detection of defects in FRP-bonded systems, particularly interfacial defects. For instance, accurate pressure wave measurement in the ultrasound regime requires direct contact to the inspected surface, therefore it is unsuitable for the remote sensing of FRP-concrete structures. Passive IRT is a remote sensing technology relying on thermal emission of the inspected object. While IRT is capable of scanning large surface areas on structures, it is still commonly perceived to be less effective in civil engineering applications where introduction of heat source to produce a pronounced difference in thermal gradients between intact and defective regions can be difficult and very challenging to achieve in the field [14]. Furthermore, the intensity of infrared images depends not only on temperature of the object, but also emissivity of the object, reflection of infrared from environmental sources, and attenuation due to atmospheric absorption [14,19]. Given the stringent requirement on temperature gradient in IRT and low resolving power, typically the technique can only pick up delamination above 20 cm in diameter [14], insufficient for detecting early-stage interfacial defects in FRP-bonded systems. Therefore, passive thermography is used to detect moisture and thermal insulation problems, rather than detecting FRP defects. Active thermography, on the other hand, requires active heating of the structure and is used instead [19]. Radar or microwave techniques are ideal for the subsurface inspection of low-loss dielectrics (e.g. dry concrete or glass fibers). Their performance in subsurface sensing will reduce when applied to lossy dielectrics (e.g. wet concrete or carbon fibers). When applied to the debonding detection problem of FRP-concrete systems, the penetration or skin depth of GHz signals may be decreased by the use of carbon fibers but still can penetrate through the thin FRP layer. However, due to the scattering nature of electromagnetic waves in the microwave spectrum, interference and scattering of reflected radar signals can make radar image interpretation challenging. In X-ray radiography, the difference in absorption of an X-ray beam through an object is imaged to detect features and defects within the object. The thickness of the defect along the direction parallel to the beam

has to be large enough in order to result in an appreciable difference in absorption [15], which does not apply to the case for interfacial defects. Furthermore, as concrete is a relatively absorptive medium for X-ray (and neutrons), a much higher beam intensity is required for imaging concrete structures when compared with other objects in medical or security applications. Proper shielding is required to avoid dangerous dosage of ionizing radiation in human and livestock [15]. Lastly, accessibility to the back surface of the object is required to obtain an X-ray image unless backscatter X-ray is used, which would limit the applicability of X-ray radiography.

To address the limitations of existing remote NDT technologies, many new constructions have turned to using embedded NDT sensors combined with finite element modeling in the field of structural health monitoring [20–24]. However, many old structures are not instrumented with embedded sensors, and the use of remote sensing technologies is ideal for condition assessment. Recently, studies investigating the combination of acoustic emission with ultrasound [25], acoustic emission with thermography [26], and thermography with ultrasound [27] have been reported. Nonetheless, in all cases at least one of the applied techniques requires direct contact with the specimen.

Given the limitations of existing NDT technologies in remote debonding detection, a combination of acoustic-laser and imaging radar techniques, both remote measurement techniques, is introduced and investigated for the remote defect detection of FRP-bonded concrete structures. The acoustic-laser technique depends only on the mechanical properties of near-surface defects and can pinpoint near-surface defects at a smaller length scale. This feature provides acoustic-laser a superior resolution over many other NDT techniques. On the other hand, the imaging radar technique utilizes the transmissibility of electromagnetic waves (radar signals) in dielectrics (e.g. FRP, concrete) and superimposes reflected radar signals in the space domain to detect/locate subsurface defects in FRP-concrete systems. The acoustic-laser technique has a higher resolution (resolution = 0.22 cm) than the imaging radar technique (resolution = 3.75 cm) in space. While the acoustic-laser technique can inspect the projected area of an interfacial defect on the surface, the imaging radar technique can inspect the volume of an interfacial defect in the subsurface. Furthermore, unlike X-ray radiography, these two techniques can identify defects of small thickness along the direction of wave propagation without requiring a safety zone behind the structure or posing any radiation hazards to human and environment.

3. Approach – acoustic-laser and radar techniques

3.1. Acoustic-laser technique

Originally conceived to detect debonding defects located at or near the interface between an FRP sheet and its substrate (interfacial defects), the acoustic-laser technique is a general NDT method for remote identification and evaluation of geometries that can be excited acoustically and can accommodate observable surface vibration [28–30]. This technique relies on the principle that an interfacial defect behaves like a drum, with both its amplitude and frequency of vibration changing significantly when compared with an intact region (i.e. bonded perfectly to the substrate) [28,31]. Reported applications include the use of a high-power standoff parametric acoustic array (PAA) to excite FRP-bonded structures and a laser Doppler vibrometer (LDV) to monitor resulting vibration [30]. In these applications, the velocity response peaks correspond to different vibration modes of a subsurface defect. In this study, the measurement setup is modified in order to demonstrate the flexibility in both deployment and commercial viability of the acoustic-laser

technique (Fig. 1). As the fundamental frequency of commonly found interfacial defects has been shown to be at the order of kHz [28], a conventional studio monitor is used as the acoustic excitation source to substitute a PAA. In order to cover a wide range of frequencies in a short period of time, white noise is used for excitation instead of a frequency sweep. Furthermore, as a tradeoff between cost and signal-to-noise ratio (SNR), the LDV measurement system is replaced by a low-cost light detection system to directly monitor the variation of reflected laser intensity, without invoking the Doppler effect. The frequency spectrum of the intensity variation is obtained via Fast Fourier Transformation (FFT) to identify vibration modes. Although the reported acoustic-laser system provides high accuracy results, the cost of the system is high due to the custom-built acoustic source [30]. The current setup, on the other hand, is relatively affordable and can provide a comparable defect detection capability using the same set of inputs (optical measurement and acoustic excitation) albeit at the expense of high environmental noise level and vibration velocity.

3.2. Imaging radar technique

In this research, an imaging radar technique using the stripmap synthetic aperture radar (SAR) monostatic mode was applied for investigating the subsurface condition of FRP-concrete cylinders. Standard stripmap SAR algorithm was adopted, while frequency-modulated continuous wave (FMCW) signals were used. In the stripmap SAR imaging method, the radar travels in a straight line (cross-range axis, r_x), transmitting and receiving electromagnetic waves in the direction (range axis, r) perpendicular to the cross-range axis. Fig. 2 illustrates the strip SAR imaging mode. Measured radar signals were first convoluted with a target amplitude function in a Fourier transform and then projected to the synthetic aperture or slow-time domain. The Fresnel approximation was used to deconvolute measured radar signals in the synthetic aperture domain. A two-dimensional matched filtering of the measured radar signals was performed with a reference signal that is calculated by a fast-time matched filter in the frequency domain. The filtered radar signals in the frequency domain were then multiplied by a phase function to become the target function of measured radar signals. Interpolation of sampled target function was needed in order to evenly reconstruct the SAR image in the space domain. Finally, an inverse Fourier transform was carried out to project the target function from the frequency domain back to the space domain, resulting in stripmap SAR images. The final back-projected SAR image amplitude $I(r, r_x)$ in the range-cross-range plane can be represented by:

$$I(r,r_x) = \int_{-\infty}^{\infty} h\left(t - \frac{2r'}{c}\right) \exp\left(-4i\pi\frac{r'}{\lambda}\right) A(r') \int_0^{R_x} S(r',r_x') a\left(\frac{r_x - r_x'}{R_0}\right)$$
$$\exp\left[-iF(r_x - r_x')^2\right] dr_x' dr' \tag{1}$$

where r = range, r_x = cross-range, h = a matched filter, t = time, $c = 3 \times 10^8$ m/s (speed of radar signals in free space), $i = \sqrt{-1}$, λ = wavelength, A = a function accounting for antenna pattern, processing gain and the range spreading loss, S = scattering amplitude, a = the two-way amplitude azimuth antenna pattern, R_0 = range location of the radar, and F = a focusing function. All SAR images reported in this paper were generated by Eq. (1). Formulation of various SAR modes can be found in [32,33] for inverse SAR mode.

4. Experimental work

4.1. Specimen description

Three cylindrical concrete specimens with a height of 300 mm and a diameter of 150 mm were fabricated with a water-to-
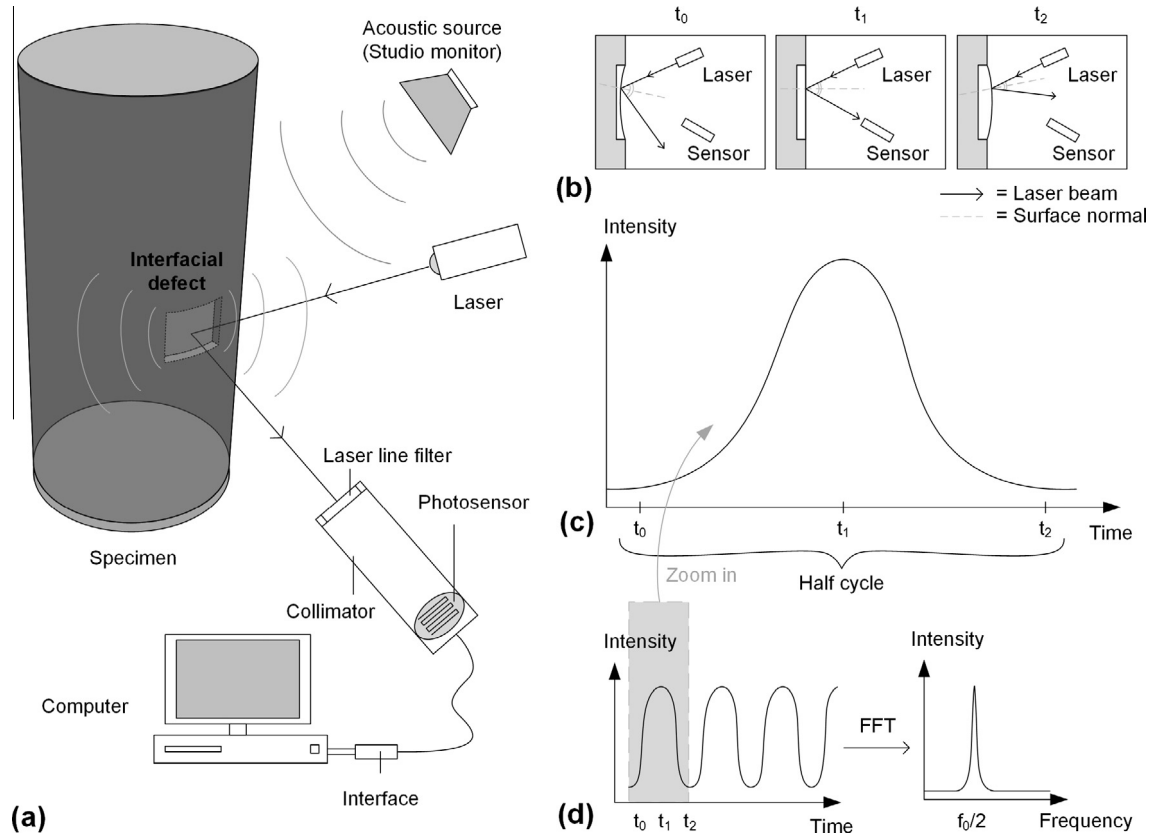
Fig. 1. Principle of the modified acoustic-laser technique. (a) The defect is acoustically excited by a studio monitor and illuminated by a laser. The intensity of reflected laser beam is measured by a detector and the signal is processed by a computer. (b) An illustration of how the intensity of the reflected laser beam is modulated by the defect vibration due to a changing surface normal. (c) The change of reflected laser beam intensity during half a cycle. (d) By converting the time-domain variation of detected laser intensity into frequency domain, the vibration frequency of the defect can be obtained.
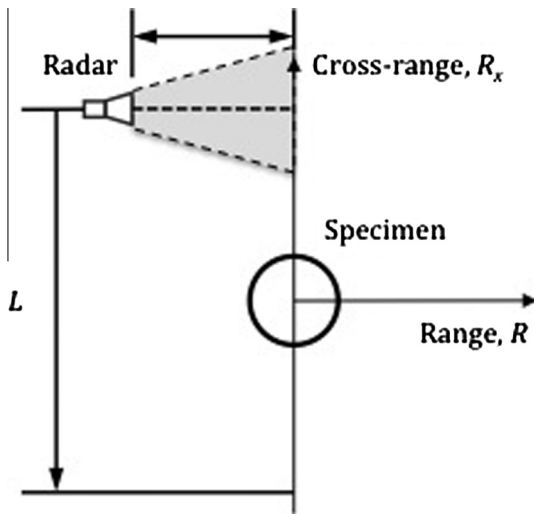
Fig. 2. Stripmap synthetic aperture radar (SAR) imaging mode.

cement ratio of 0.6 (Fig. 3). In each specimen, an interfacial defect was introduced artificially (a nomenclature of three specimens is introduced in Table 1). The interfacial defect was created by inserting a thin piece of square Styrofoam placeholder on the cylindrical mold surface. The Styrofoam piece was removed before FRP-bonding, leaving an air gap at the interface between FRP and concrete. The specimens were moist-cured for 28 days, sanded to prepare the surface for FRP bonding, and dried in an oven for 3 days

before bonding 3 layers of carbon FRP wrap using epoxy. The specimens were then cured for an additional 7 days before measurement.

4.2. Near-surface acoustic-laser measurements

Three FRP-concrete specimens were acoustically excited by a studio monitor and locally measured by a continuous wave diode laser to collect the resulting vibration. The excitation was an acoustic white noise with sample rate of 48 kHz over a period of 10 s at 88.5 dB$_{SPL}$ (using a reference sound pressure of 20 μPa) with the environmental noise level between 70 and 75 dB$_{SPL}$. The laser operated at 80 mW with a wavelength of 532 nm. As the laser wavelength is not critical to measurement, other laser wavelengths or laser power levels can be used in compliance of specific safety requirement (e.g. eye-safe lasers). A reflective sticker was attached onto the point of measurement to enhance reflectivity of the surface as well as to smooth out the effect of surface variation across specimens. For extended measurement range, the use of retroreflective stickers is preferred for further enhancement in reflectivity and SNR. However, the carbon FRP surface is sufficiently glossy and reflective for measurement and the use of a reflective sticker is not necessary in ordinary circumstances. The reflection of the laser beam from the FRP surface was recorded by a custom-built photodetector. The variation of the reflected laser intensity was transformed into the frequency domain using FFT and the Blackman–Harris windowing function, which is shown in Fig. 4. The noise floor was defined to be the median of the spectrum such that no control measurement of intact specimen is required, and a cutoff frequency at 500 Hz was chosen to account for low frequency
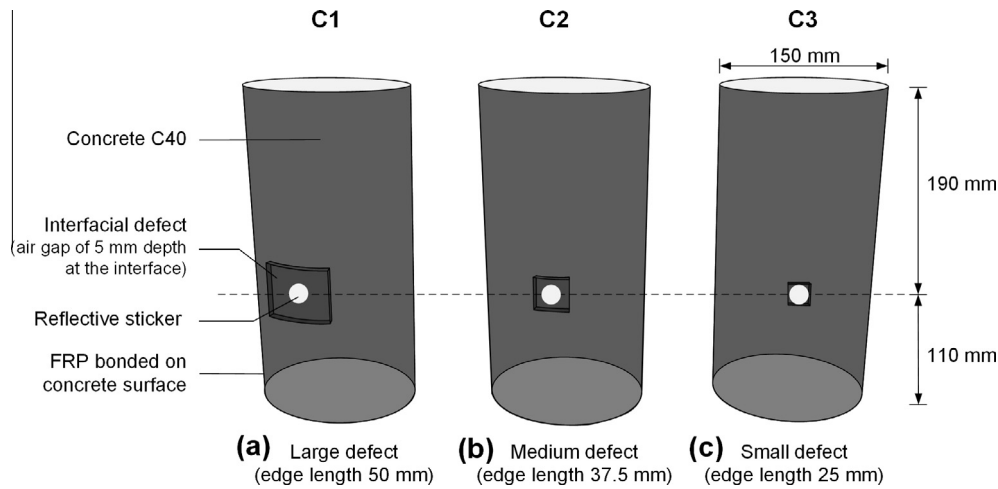
Fig. 3. Schematic diagram of three specimens containing defects.

Table 1
Defect dimensions in the specimens. Each specimen has an interfacial defect.

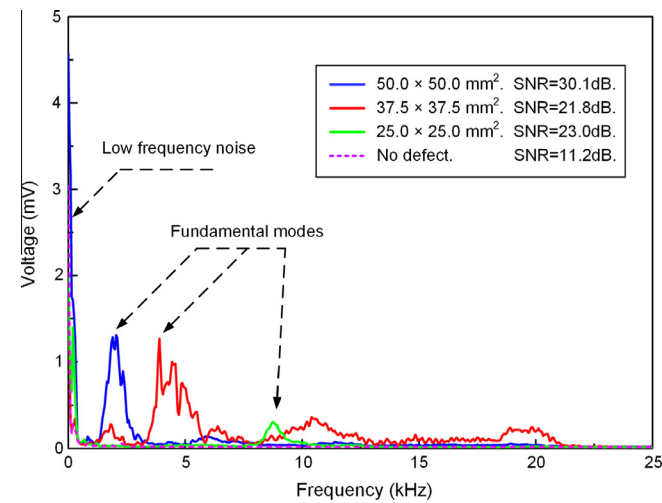| Specimen	C1	C2	C3
Interfacial defect ($W \times H \times D$ mm³)	$50 \times 50 \times 5$	$37.5 \times 37.5 \times 5$	$25 \times 25 \times 5$

Fig. 4. Light intensity measurement in terms of voltage measured is plotted in frequency domain. The peaks are visible with SNR ranging from 21.8 dB to 30.1 dB. A general trend that a larger defect would result in a lower resonance frequency is observed. Low frequency noise below 500 Hz is prominent and is ignored from all calculations, but it did not obscure the identification of response peaks.

noise. The acoustic excitation was 99.3 dB$_{SPL}$, for 5 s, and the resulting SNR ranged from 21.8 dB to 30.1 dB. The SNR was defined as the peak divided by the median of the frequency response above 500 Hz. The source of low frequency noise is present in both the defective region and the intact region (control), which enables its elimination. Possible causes include pink noise, electromagnetic interference from 50 Hz mains electricity delivery, the vibration of concrete specimens, and the vibration of measurement equipment. Generally speaking, a larger interfacial defect results in a lower fundamental frequency as we observed. The specimens exhibited a strong inverse relationship between the defect's fundamental mode and its area ($R^2 = 0.9996$), suggesting that defect area can be inferred from the measured fundamental mode. At present

the acoustic-laser technique only measures interfacial defects and is not designed to detect interior defects deep inside the concrete substrate.

4.3. Subsurface radar images

A custom-built imaging radar system was used to investigate the subsurface condition of FRP-concrete cylinder specimens. Two inspection schemes were applied in the radar imaging of all specimens; normal incidence and oblique incidence. In the normal incidence scheme, the radar moves on cross-range axis in parallel to the longitudinal axis of FRP-concrete cylinder, as shown in Fig. 5. In the oblique incidence scheme, the radar moves on the cross-range axis at an angle (θ) to the longitudinal axis of FRP-concrete cylinder. In other words, the normal incidence scheme is a special case of the oblique incidence scheme when $\theta = 0°$. Three FRP-concrete cylinders were scanned by the imaging radar system using a FMCW signal with a carrier frequency at 10.5 GHz. All radar images were produced in an electromagnetically anechoic chamber in the Department of Civil and Environmental Engineering at UMass Lowell (Fig. 6). The chamber was designed to conduct electromagnetic measurements in the frequency range of 0.5–18 GHz. In all SAR images, the direction of radar movement was the cross-range axis. Generated SAR images of all FRP-concrete cylinders at $\theta = 25°$ are shown in Figs. 7–9. In Figs. 7–9, white dashed lines indicate the location of CFRP-concrete cylinders and the location of an interfacial defect.

In Figs. 7–9, all SAR images of intact specimens are considered as the background signal (or noise). In the SAR images of damaged specimens, scattering signals are reconstructed at or near the location of a subsurface/interfacial defect and used to indicate the presence of the defect. In this paper, the intensity and distribution of scattering signals can change with the variation of incident angle and defect size.

4.4. Debonding detection

4.4.1. Acoustic-laser technique

For the acoustic-laser technique, a thresholding method was applied to identify interfacial defects. A signal in a frequency plot (similar to Fig. 4) above a certain threshold value, to be determined from field tests, would indicate the existence of a defect at the measurement point. If an LDV were used for vibration measurement, the quantity measured would be the vibration velocity normal to the direction of the laser beam. With the knowledge of
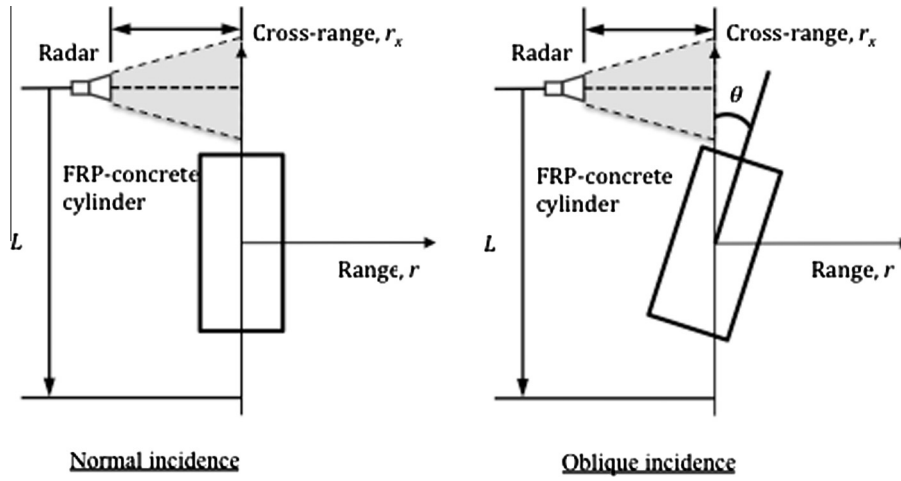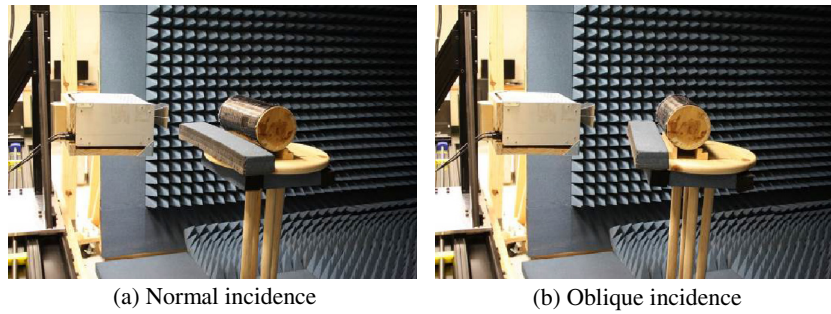
Fig. 5. Normal and oblique incidence schemes.

(a) Normal incidence   (b) Oblique incidence

Fig. 6. Normal and oblique incidence measurement schemes inside the electromagnetic anechoic chamber at UMass Lowell.
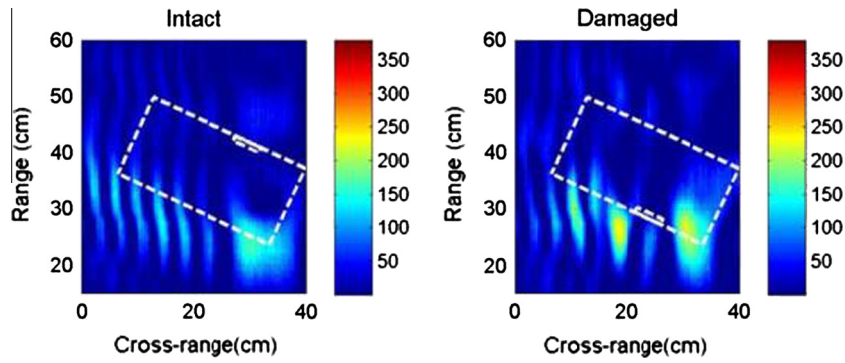

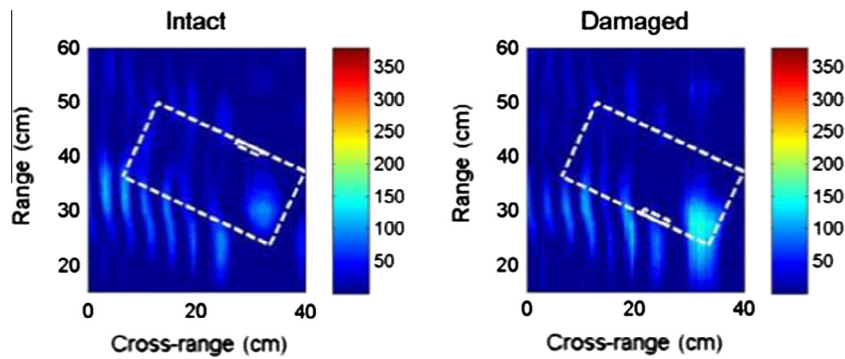**Fig. 7.** Specimen C1, debonding defect, oblique incidence, 25-deg.

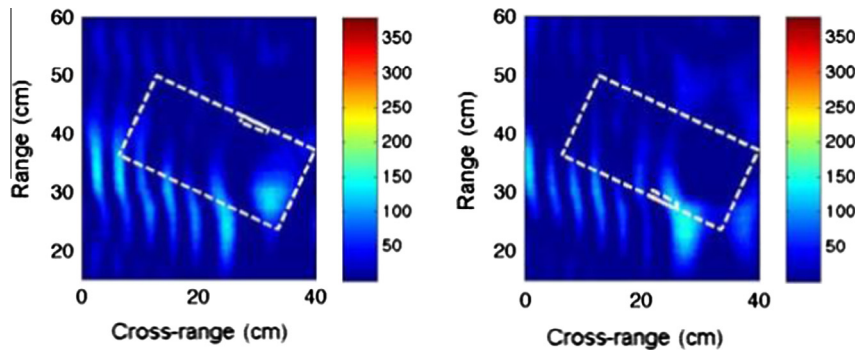**Fig. 8.** Specimen C2, debonding defect, oblique incidence, 25-deg.

Fig. 9. Specimen C3, debonding defect, oblique incidence, 25-deg.

vibrational behaviors of FRP-bonded specimens, a threshold vibration velocity can be obtained by a compromise between minimizing the rate of false positives (reporting of a defect when there is none) and minimizing the rate of false negatives (failure to detect a defect when there is one) based on field test results. It is suggested that emphasis should be placed on minimizing false positives since the occurrence of defect is rare in practical applications, i.e. number of intact areas measured is much greater than the number of defect areas [34]. In this study, however, a modified acoustic-laser technique was used in which the measured quantity is reflected laser intensity rather than vibration velocity. As the explicit governing equation between the measured amplitude and the physical quantity of the defect is yet to be found, the measured response of a suspected defect is a relative quantity with only the frequency dependence. Therefore, defect detectability is represented by SNR, using the technique of thresholding. A SNR threshold was chosen from the results such that a defect is deemed to exist at a measurement point if its signal is above this threshold value. As seen in Fig. 4 the SNR of defected specimens ranges from 21.8 dB to 30.1 dB, with the control amplitude fluctuating no more than 11.2 dB from the median of the spectrum. Hence, given the adopted experimental configuration in this study, a SNR threshold was chosen between 11.2 dB and 21.8 dB. This selection of SNR threshold results in neither false positive nor false negative in the detection of response peaks for vibration frequencies above 500 Hz. Due to clear response in laboratory settings and the limited number of specimens, a receiver operating characteristic (ROC) curve cannot be developed as a threshold can be chosen such that the detection rate is 100%. Nonetheless, it is expected that a compromise between false positive rate and false negative rate is needed in practical applications. In general, it is recommended that (i) the measurement system should be calibrated in the field, (ii) the noise level should be determined, and (iii) the presence of low frequency noise, particularly optical noise due to flickering ambient light, should be measured. Once a detection threshold and a low cut-off frequency are chosen based on the aforementioned recommendations, interfacial defects can be identified using this low-cost acoustic-laser technique. The same threshold can be used as long as the measurement setup, the FRP material and the underlying geometry of the measured structure remain the same.

4.4.2. Imaging radar technique

For the use of an imaging radar system to detect FRP debonding in concrete specimens, changes of scattering radar signals (SAR amplitude) were used for detecting and locating subsurface FRP debonding. The principle of detection is based on the fact that, when there is a FRP debonding area in an FRP-concrete specimen, the interfaces (FRP-to-air, air-to-concrete) will produce scattering signals to be measured by the radar system, due to the dielectric

contrast between two materials. These scattering radar signals are eventually integrated by the stripmap SAR imaging algorithm (Eq. (1)) and rendered into significant increases of SAR amplitude in the SAR images of FRP-concrete specimens. It is such changes in SAR amplitude that the imaging radar technique utilizes to indicate and to locate the presence of subsurface anomalies in a multilayer system [33]. In general, SAR amplitude is affected by background geometry (e.g. surface roughness, corners), material's electromagnetic property, inspection angle, and inspection distance/range for intact structures. On the other hand, defect geometry, defect location, defect orientation, electromagnetic property of the defect can affect the SAR amplitude of scattering signals (used for damage detection) in damaged structures. In other words, there exists an optimal combination of measurement parameters (e.g. frequency, angle, distance, bandwidth) to achieve the best detectability for a given defect.

From the result we have obtained, the SAR amplitudes along the front surface were extracted from Figs. 7–9 for both the intact and the damaged sides of an FRP-concrete cylinder for comparison and shown in Figs. 10–12. Fig. 10 shows these SAR curves for specimen C1, and the actual location of an artificial defect is indicated by its edges in the figure. Figs. 11 and 12 illustrate the results for specimens C2 and C3, respectively. The inspection angle was 25-deg in all these figures.

In Figs. 10–12, it is observed that, according to the principle of detection using SAR imaging, the SAR amplitude of damaged curves must be greater than the one of intact curves to indicate the presence of a subsurface defect. This is the case for specimens C1 and C2 but not for specimen C3, indicating that the defect in specimen C3 is undetectable at $\theta = 25°$. This also suggests that the signal-to-noise ratios (SNR) in Figs. 10 and 11 are greater than the one in Fig. 12.
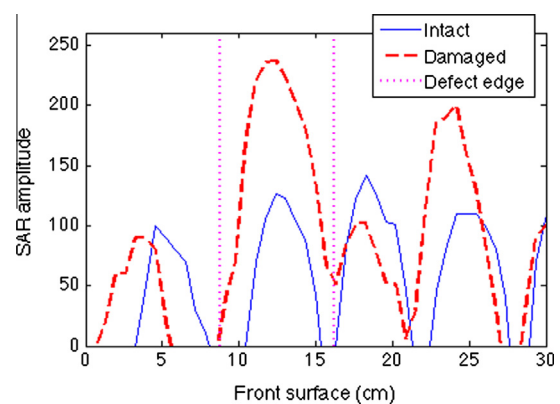

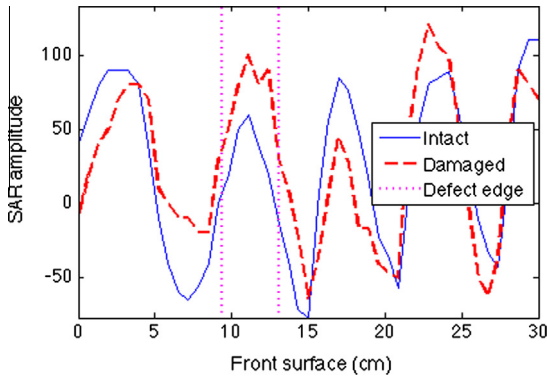**Fig. 10.** Specimen C1, front surface SAR amplitude curves, 25-deg.

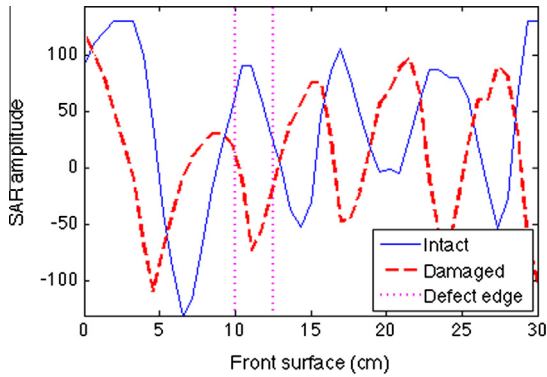**Fig. 11.** Specimen C2, front surface SAR amplitude curves, 25-deg.

Fig. 12. Specimen C3, front surface SAR amplitude curves, 25-deg.

Since the stripmap SAR images are angle-dependent in this research. SNR at various inspection angles were also studied in this research. In this paper, radar detectability of subsurface defect is quantified by a signal-to-noise ratio, SNR_R, defined by:

$$\mathrm{SNR_R}(\theta) = \frac{[I_{\mathrm{dam}}(\theta)]_{\max}}{[I_{\mathrm{int}}(\theta)]_{\mathrm{avg}}} \qquad (2)$$

where θ is the incident angle (deg.), $[I_{\mathrm{dam}}(\theta)]_{\max}$ the maximum SAR amplitude of the surface SAR amplitudes on a damaged specimen, and $[I_{\mathrm{int}}(\theta)]_{\mathrm{avg}}$ the average SAR amplitude of the surface SAR amplitudes on a intact specimen. In this definition, $[I_{\mathrm{int}}(\theta)]_{\mathrm{avg}}$ is the average SAR amplitude on the front surface of an intact specimen and represents all background effects. $[I_{\mathrm{dam}}(\theta)]_{\max}$ represents the maximum scattering signal indicating the location of defect. Fig. 13 shows the calculated $SNR_R(\theta)$ values for specimens C1–C3 in the angular range of $\theta \in [0, 15, 20, 25, 30, 35, 45, 60]$ (in degrees).

It is found that, given a constant inspection distance/range (=40 cm), SNR_R increases at the inspection angles where scattering SAR amplitude ($[I_{\mathrm{dam}}(\theta)]_{\max}$) becomes stronger than background SAR amplitude ($[I_{\mathrm{int}}(\theta)]_{\mathrm{avg}}$). For the $50 \times 50 \times 5$ (mm) defect (C1), 45-deg was found to be the optimal inspection angle, while 20-deg came closely second. For $37.5 \times 37.5 \times 5$ (mm) defect (C2), 25-deg was found to be the optimal inspection angle. For the $25 \times 25 \times 5$ (mm) defect (C3), 35-deg was found to be the optimal inspection angle. To verify these findings, front-surface SAR amplitude curves at the optimal inspection angles for specimens C1–C3 are provided in Figs. 14–16, respectively. In Figs. 14–16, the maximum amplitude of the damaged SAR curves coincides or locates very close to the edge of the defect as expected. In addition, the SAR amplitudes of a damaged FRP-concrete cylinder are all greater than the ones of an intact FRP-concrete cylinder, due to the com-
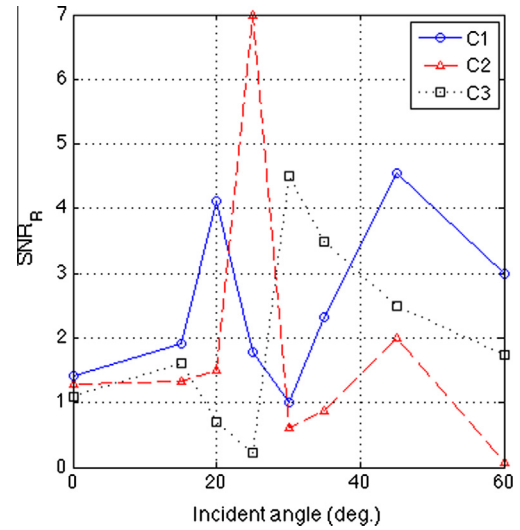

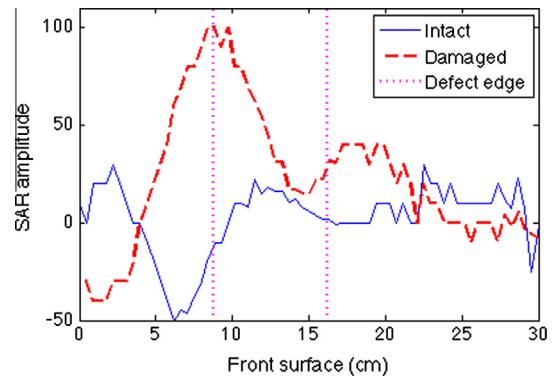**Fig. 13.** SNR_R of SAR amplitudes for three specimens at eight inspection angles.

Fig. 14. Specimen C1, front surface SAR amplitude curves, optimal inspection angle (45-deg.).
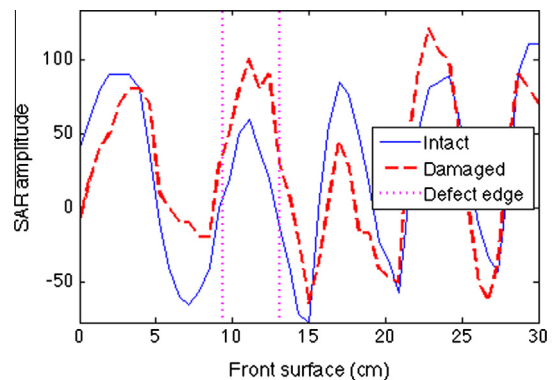

Fig. 15. Specimen C2, front surface SAR amplitude curves, optimal inspection angle (25-deg.).

bined effects of wave scattering and change in the dielectric properties of FRP-concrete.

4.4.3. Comparison between two techniques in defect detection

It is observed that a single interfacial defect can result in measurable changes of both the mechanical and dielectric properties of the FRP-bonded concrete system. The acoustic-laser technique provides a local measurement based on the changes in vibrational
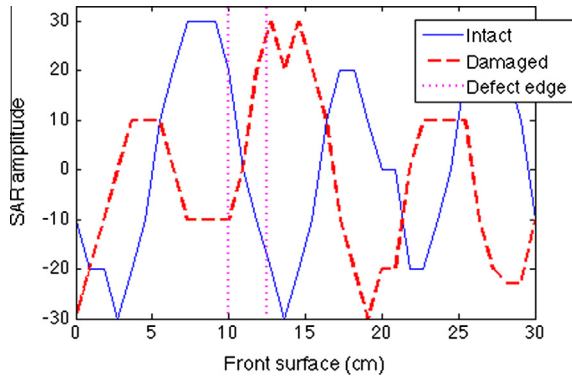
Fig. 16. Specimen C3, front surface SAR amplitude curves, optimal inspection angle (35-deg.).

properties of the specimens, while the imaging radar provides a global measurement that relies on the changes in dielectric properties. It is suggested that, in practice, the two techniques can work in tandem, i.e. the imaging radar can detect the existence of defect(s) in a region, and the acoustic-laser can locate the defect (s) within the region. It should be noted that the most relevant change in properties towards the integrity of the FRP-bonded concrete system is its change in mechanical properties. The extent of damage, in terms of the defect area, can be estimated from the peak frequency of the acoustic-laser measurement based on the plate theory [30]. Given the material properties, the area of damage can be estimated using finite element method on a cylindrical surface, or directly from the plate theory on a planar surface [28]. Regarding the latter case, for a square interfacial defect of thickness h, volumetric density ρ and area A, its vibration modes $\omega_{l,m}$ are given by:

$$\omega_{l,m} = \frac{\lambda_{l,m}}{A}\sqrt{\frac{D}{\rho h}} \tag{3}$$

whereas for a circular defect of radius r,

$$\omega_k = \sqrt{\frac{D}{\rho h}}\left(\frac{s_{i,k}}{r}\right)^2 \tag{4}$$

where $D = \frac{Eh^3}{12(1-v^2)}$ is the bending stiffness; E is the Young's modulus; v is the Poisson's ratio of the plate; $\lambda_{l,m}$ is a numerically calculated constant for each vibration mode l and m with $\lambda_{1,1} \sim 35.99$; and $s_{i,k}$ is the kth root of the equation $J_i(s)I_{i+1}(s) + J_{i+1}(s)I_i(s) = 0$, in which $J_i(s)$ and $I_i(s)$ are the ith order Bessel function and modified Bessel function of the first kind, respectively, for i being a non-negative integer. The inverse relationship between vibration frequency and defect area allows a defect area to be calculated from the frequency response of a specimen.

For the acoustic-laser technique, the minimum detectable size varies depending on definition of SNR threshold as well as the specific setup used. From Eqs. (3) and (4) it can be seen that the measurable range of acoustic-laser technique depends not only on the area of the defect, but also on bending stiffness, thickness, and density of the FRP. Fortunately, these parameters are constant for each specimen. As the measurement is conducted in frequency domain, the bandwidth (sampling frequency) of the data acquisition device is also relevant to the minimum detectable size. Lastly, there is the factor of environmental noise which influences SNR. For the particular acoustic-laser setup used in this paper, the minimum detectable defect size is around 2×2 cm^2, with the bottleneck being measurement bandwidth. Depending on specific

setup, however, the detectible defect size can vary by many orders of magnitude.

The structural health of FRP-bonded concrete systems can be monitored more effectively and efficiently through adopting the combination of both acoustic-laser and radar techniques. A reasonable SNR ratio for both techniques has been demonstrated experimentally, which can ensure the effectiveness of our proposed scheme. In addition, the global radar approach can figure out possible interfacial defect locations in a timely manner through several scans. After determining the problematic region through the radar scan, the local acoustic laser approach can be used to detect the location and size of the defect through the vibrational behavior of the bonded system, resulting in a much more efficient inspection process.

5. Conclusion

In this study, the acoustic-laser and the imaging radar techniques, though complementary in their measurement results, have very different setups. In the acoustic-laser technique, acoustic excitation source and optical measurement are separated but coupled. In the imaging radar technique, wave transmission and receiving are carried out by single radar antenna. As such, there are consequences in cost, transportation, and ease of use. However, the light source used in the acoustic-laser technique can be of various wavelengths, include microwave. Thus it is plausible that the optical hardware from the acoustic-laser technique can be merged with the imaging radar technique, resulting in a simplified setup consisting only of a modified radar sensor and an acoustic excitation source (e.g. a loudspeaker), while providing similar capabilities. Remote sensing techniques such as acoustic-laser and imaging radar have provided civil engineers a promising and versatile approach to assess the condition of structures. The acoustic-laser technique measures the local, mechanical response on the surface of structures, while the imaging radar technique measures the global, electromagnetic response on the surface and subsurface of structures. In addition, our current work forms a basis to understand the relationship between mechanical and dielectric behaviors with the existence of an interfacial defect. Our other research findings are concluded in the following.

1. Detectability of the imaging radar technique depends on background characteristics (e.g. geometry, material's property), inspection scheme (e.g. angle, distance/range, frequency), and defect characteristics (e.g. size, shape, orientation). In this paper, radar detectability is quantified by a signal-to-noise ratio SNR$_R$ (Eq. (2)).
2. In the SAR images of damaged specimens, scattering radar signals are reconstructed at or near the location of a subsurface/interfacial defect and used to indicate the presence of the defect. In our experimental SAR imaging result of CFRP-concrete specimens, the presence of scattering signals in SAR images indicates the presence of a subsurface anomaly. The amplitude of the scattering signals increases with the increase of anomaly size. The maximum amplitude of the scattering signals also suggests the location of the anomaly (Figs. 10–12). Meanwhile, optimal inspection angle depends on (i) the geometry and size of subsurface anomaly, (ii) surface roughness of the background, and (iii) distribution of dielectric properties in the background and the anomaly (dielectric contrast).
3. Characteristics of background information are important when inspecting subsurface defects using the imaging radar technique on civil engineering structures. This is because that, the SAR images of structures can be affected by geometry, or surface roughness, or dielectric property change, or combinations

of all factors. Background subtraction remains an efficient approach when all other factors are unknown or difficult to collect them all.

4. When using SAR images for defect size determination, larger defects usually create scattering signals with higher amplitudes. This is the case when comparing Fig. 10 (defect size = $50 \times 50 \times 5$ mm^3) and Fig. 11 (defect size = $37.5 \times 37.5 \times 5$ mm^3). In Fig. 10, the SAR amplitude of a $50 \times 50 \times 5$ mm^3 defect is 241. In Fig. 11, the SAR amplitude of a $50 \times 50 \times 5$ mm^3 defect is 100.

5. The modified acoustic-laser technique can reliably detect interfacial defects at SNR ranging from 21.8 to 30.1 dB, despite the use of low-cost components. A general trend is observed that, for the same material, a larger defect area will result in both a higher SNR and a lower fundamental mode frequency.

6. As the acoustic-laser technique operates at microwave frequencies as well, the setups of the two techniques can be combined and simplified in future studies. The time-domain variation from the radar signal scattered by an acoustically-excited specimen can be recorded and processed in the frequency domain to obtain the frequency response of the specimen, such that frequency response data similar to Fig. 4 will be available for each point on the radar image.

Acknowledgements

References

[1] ACI Committee 440, Institute AC, Guide for the Design and Construction of Externally Bonded FRP Systems for Strengthening Concrete Structures, American Concrete Institute, 2008.

[2] Canadian Standard Association, Design and Construction of Building Components with Fibre Reinforced Polymers, S806-02, Canadian Standards Association International, Toronto, Canada, 2002.

[3] ACI Committee 318–05, Institute AC. Building Code Requirements for Structural Concrete (ACI 318–05) and Commentary (ACI 318R–05), American Concrete Institute USA, 2005.

[4] Y.-Y. Wei, Y.-F. Wu, Unified stress–strain model of concrete for FRP-confined columns, Constr. Build. Mater. 26 (1) (2012) 381–392.

[5] O. Büyüköztürk, D. Lau, C. Tuakta, Durability and long-term performance modeling of frp-concrete systems. The 6th International Conference on FRP Composites in Civil Engineering-CICE2012.

[6] O. Gunes, D. Lau, C. Tuakta, O. Büyüköztürk, Ductility of FRP–concrete systems: investigations at different length scales, Constr. Build. Mater. 49 (2013) 915–925.

[7] T. Jiang, J. Teng, Theoretical model for slender FRP-confined circular RC columns, Constr. Build. Mater. 32 (2012) 66–76.

[8] R. Realfonzo, A. Napoli, Confining concrete members with FRP systems: predictive vs design strain models, Compos. Struct. 104 (2013) 304–319.

[9] M.F. Fahmy, Z. Wu, Evaluating and proposing models of circular concrete columns confined with different FRP composites, Compos. B Eng. 41 (3) (2010) 199–213.

[10] T.M. Pham, L.V. Doan, M.N. Hadi, Strengthening square reinforced concrete columns by circularisation and FRP confinement, Constr. Build. Mater. 49 (2013) 490–499.

[11] C.G. Bailey, M. Yaqub, Seismic strengthening of shear critical post-heated circular concrete columns wrapped with FRP composite jackets, Compos. Struct. 94 (3) (2012) 851–864.

[12] A. Muntasir Billah, M. Shahria Alam, Seismic performance of concrete columns reinforced with hybrid shape memory alloy (SMA) and fiber reinforced polymer (FRP) bars, Constr. Build. Mater. 28 (1) (2012) 730–742.

[13] O. Büyüköztürk, H.C. Rhim, Radar measurements of concrete for nondestructive evaluation of dams. Nondestructive Evaluation of Aging Infrastructure: International Society for Optics and Photonics, 1995. p. 168–174.

[14] M.R. Clark, D.M. McCann, M.C. Forde, Application of infrared thermography to the non-destructive testing of concrete and masonry bridges, NDT and E Int. 36 (4) (2003) 265–275.

[15] D.M. McCann, M.C. Forde, Review of NDT methods in the assessment of concrete and masonry structures, NDT and E Int. 34 (2) (2001) 71–84.

[16] R.D. Owen, Portable linear accelerators for X-ray and electron-beam applications in civil engineering, NDT and E Int. 31 (6) (1998) 401–409.

[17] J.S. Popovics, J.L. Rose, A survey of developments in ultrasonic Nde of concrete, IEEE Trans. Ultrason. Ferroelectr. Freq. Control 41 (1) (1994) 140–143.

[18] T. Saarenketo, T. Scullion, Road evaluation with ground penetrating radar, J. Appl. Geophys. 43 (2–4) (2000) 119–138.

[19] A. Kylili, P.A. Fokaides, P. Christou, S.A. Kalogirou, Infrared thermography (IRT) applications for building diagnostics: a review, Appl. Energy 134 (2014) 531–549.

[20] D.E. Adams, Health Monitoring of Structural Materials and Components: Methods with Applications, John Wiley & Sons, Chichester, England; Hoboken, NJ, 2007.

[21] Y.-L. Xu, Y. Xia, Structural Health Monitoring of Long-span Suspension Bridges, Spon Press, Abingdon, Oxon; New York, 2012.

[22] T. Chan, D.P. Thambiratnam, Structural Health Monitoring in Australia, Nova Science Publishers, New York, 2011.

[23] B. Glisic, D. Inaudi, Fibre Optic Methods for Structural Health Monitoring, John Wiley & Sons, Chichester, West Sussex, England; Hoboken, NJ, 2007.

[24] J. Leng, A. Asundi, Structural health monitoring of smart composite materials by using EFPI and FBG sensors, Sensor Actuator A Phys. 103 (3) (2003) 330–340.

[25] D.G. Aggelis, N.M. Barkoula, T.E. Matikas, A.S. Paipetis, Acoustic structural health monitoring of composite materials: damage identification and evaluation in cross ply laminates using acoustic emission and ultrasonics, Compos. Sci. Technol. 72 (10) (2012) 1127–1133.

[26] E.Z. Kordatos, D.G. Aggelis, T.E. Matikas, Monitoring mechanical damage in structural materials using complimentary NDE techniques based on thermography and acoustic emission, Compos. Part B-Eng. 43 (6) (2012) 2676–2686.

[27] D.G. Aggelis, E.Z. Kordatos, D.V. Soulioti, T.E. Matikas, Combined use of thermography and ultrasound for the characterization of subsurface cracks in concrete, Constr. Build. Mater. 24 (10) (2010) 1888–1897.

[28] T.K. Cheng, D. Lau, Vibrational characteristics of FRP-bonded concrete interfacial defects in a low frequency regime. SPIE Smart Structures and Materials+ Nondestructive Evaluation and Health Monitoring: International Society for Optics and Photonics, 2014. p. 90630R-R-11.

[29] D. Lau, One dimensional predictive model of interfacial stiffness in FRP-bonded concrete system using acoustic-laser technique. SPIE Smart Structures and Materials+ Nondestructive Evaluation and Health Monitoring: International Society for Optics and Photonics, 2013. p. 86940W-W-6.

[30] T.-Y. Yu, R. Haupt, Damage inspection of fiber reinforced polymer-concrete systems using a distant acoustic-laser NDE technique. SPIE Smart Structures and Materials+ Nondestructive Evaluation and Health Monitoring: International Society for Optics and Photonics, 2010. p. 76491J-J-8.

[31] Q. Qiu, D. Lau, Experimental evaluation on the effectiveness of acoustic-laser technique towards the FRP-bonded concrete system. SPIE Smart Structures and Materials+ Nondestructive Evaluation and Health Monitoring: International Society for Optics and Photonics, 2015. p. 943705–10.

[32] M. Soumekh, Synthetic Aperture Radar Signal Processing, Wiley, New York, 1999.

[33] T.-Y. Yu, Distant damage-assessment method for multilayer composite systems using electromagnetic waves, J. Eng. Mech. 137 (8) (2011) 547–560.

[34] J.G. Chen. Detection of defects in FRP-reinforced concrete with the acoustic-laser vibrometry method [S m]: Massachusetts Institute of Technology, 2013.